Enhanced intrapulse difference frequency generation in the mid-infrared by a spectrally dependent polarization state

Q. Bournet, F. Guichard, M. Natile, Y. Zaouter, M. Joffre, A. Bonvalet, I. Pupeza, C. Hofer, F. Druon, Marc Hanna, et al.

Enhanced intrapulse difference frequency generation in the mid-IR by spectrally-dependent polarization state

Q. Bournet[1,2,*], F. Guichard[2], M. Natile[2], Y. Zaouter[2], M. Joffre[3], A. Bonvalet[3], I. Pupeza[4,5], C. Hofer[4,5], F. Druon[1], M. Hanna[1], and P. Georges[1]

[1] Université Paris-Saclay, Institut d'Optique Graduate School, CNRS, Laboratoire Charles Fabry, 91127, Palaiseau, France
[2] Amplitude, 11 Avenue de Canteranne, Cité de la Photonique, 33600 Pessac, France
[3] Laboratoire d'Optique et Biosciences, Ecole Polytechnique, CNRS, INSERM, Institut Polytechnique de Paris, 91128 Palaiseau, France
[4] Max-Planck-Institut für Quantenoptik, Hans-Kopfermann-Str. 1, 85748 Garching, Germany
[5] Fakultät für Physik, Ludwig-Maximilians-Universität München, Am Coulombwall 1, 85748 Garching, Germany
[*] Corresponding author: quentin.bournet@institutoptique.fr

Compiled November 24, 2021

We present a technique to optimize the intrapulse difference frequency generation efficiency for mid-IR generation. The approach employs a multi-order waveplate that is designed to selectively rotate the polarization state of the incoming spectral components on the relevant orthogonal axes for subsequent nonlinear interaction. We demonstrate a significant increase of the mid-IR average power generated by a factor $\geq$ 2.5 compared to the conventional scheme, due to an optimally distributed number of photons enrolled in the difference frequency generation process.

http://dx.doi.org/10.1364/ao.XX.XXXXXX

Intrapulse difference frequency generation (iDFG) [1–3] is a particularly simple and efficient way to generate large bandwidth and carrier-envelope phase (CEP) stable mid-IR radiation, when a sufficiently broad input spectrum is available. In the past few years, it has received renewed attention due to two recent technical achievements. First, few-cycle pulses at high repetition rate are now available due to the recent development of efficient nonlinear compression schemes of ultrafast sources at either 1 μm [4, 5], or at longer wavelength [6–8]. This allows covering the whole mid-IR range from 4 to 20 μm through iDFG, at unprecedented average power. These table-top sources are now brighter than infrared beamlines in large scale synchrotron facilities [7, 8]. Second, the fabrication of large bandgap nonlinear crystals transparent in the mid-IR, in particular $LiGaS_2$ (LGS) is reaching increased maturity. This material exhibits a large damage threshold ($\sim$1 TW/cm^2) [9], low residual and two photon absorption at the pump wavelength, and broadband phase matching around 8 μm when pumped at 1030 nm [10]. A number of experiments have been recently reported, showing excellent results [9, 11–14]. On the other hand, for longer pump wavelength, the reduced photon energy allows a more efficient conversion to the mid-IR while detrimental two photon absorption is almost negligible, thus allowing to use crystals with lower bandgaps but higher nonlinear coefficients [7, 8, 15, 16]. In all these crystals, the experiments make use of type I phase-matching configuration where the input pulse for iDFG must be split between two orthogonal polarization states. This is done by sending a linear polarization state oriented at 45° from the interaction axes [2, 3]. However, in this configuration, half of the photons corresponding to the pump and the signal waves do not contribute to the nonlinear interaction: phase matching is only achieved when the pump (short wavelength side) and signal (long wavelength side) exhibit orthogonal polarization states. To further enhance the generation efficiency, a possible trade off is to detune the pump-to-signal splitting ratio in order to increase the pump intensity, at the expense of a reduced signal intensity [17, 18]. Another more efficient solution is adding a specially designed multi-order waveplate that maximizes the use of photons by selectively rotating the input linear polarization to the interaction axes of interest based on their wavelengths: the high energy (pump) photons and the low energy (signal) photons available for the iDFG interaction are selectively rotated to the phase-matched configuration. This concept was demonstrated before [19, 20] in different contexts: in [19], it was applied to the generation of pulses at a center wavelength of 2 µm in BBO, which is not relevant for MIR applications. The technique is only mentioned in [20], in the context of a very specific optical parametric amplifier setup aiming at tailoring the input spectrum for the DFG process. In both cases it was performed with Ti:Sa based sources at 3 kHz and 1 kHz repetition rate.

In this Letter, we perform an in-depth study of this optimization, employing a multi-order waveplate designed to act as a wavelength-dependent polarization rotator and demonstrate that this simple technique allows an increase in NIR to mid-IR conversion efficiency by a factor $\geq$2.5.

The scheme of the iDFG experiment is shown in Fig. 1. It is driven by a high-energy Yb-doped-fiber amplifier delivering 200 μJ pulses at a central wavelength of 1030 nm and at a repetition rate of 250 kHz, corresponding to an average power of 50 W. The pulse duration is 260 fs. The M^2 beam quality factor measured at the output of the laser is 1.3 x 1.2. To broaden the spectrum of the pulses, the system is followed by a 70 % high-efficiency dual-stage nonlinear compression scheme, simi-

lar to the setup presented in [4]. The first nonlinear compression stage is based on a gas-filled multipass cell and chirped mirrors that compresses the pulses down to 43 fs. It is then sent to a second nonlinear compression stage based on a 350 μm diameter 1 m-long capillary and dispersive mirrors. The pulse duration is characterized using a d-scan system [21], and exhibits a pulsewidth of 10.3 fs and a total average power of 34.5 W. To avoid too high intensity on the crystal, we only used a fraction of the total output power by using a 80/20 beamsplitter.

Prior to the mid-IR generation, an additionnal 90/10 beamsplitter is inserted to use 10% of the energy as a gate for electro-optic sampling (EOS) [3, 9, 22]. 90% of the energy is used for the mid-IR generation stage which is composed of a calcium fluoride plate to optimize compression of the input pulse prior to the DFG stage, a bichromatic waveplate (BWP) oriented with an angle of 45° between its axis and the input beam polarization, an AR 900-1100 nm (R<1%) and 4-8 μm (R<4%) coated LGS crystal for iDFG, and a dichroic mirror that filters out the 1030 nm beam. The coated LGS crystal is 1-mm-thick and cut in the XY plane at an angle θ of 90° and ϕ of 44.1°. This corresponds to phase matching for a pump beam at 900 nm polarized along the XY plane (later denoted as e for extraordinary) and signal beam at 1100 nm along the Z direction (later denoted as o for ordinary). The idler beam in the mid-IR is polarized along the e direction. The total average power incident on the LGS crystal is 19.7 W (79 μJ) with a $1/e^2$ diameter of 3.6 mm, corresponding to an estimated peak intensity of 150 GW/cm^2.

For the EOS characterization, the s-polarized mid-IR and the p-polarized gate beams are spatially recombined with a 2-7 μm antireflection coated germanium (Ge) plate. Both beams are focused by a first 100 mm focal-length off-axis parabolic mirror and propagate collinearly through a 30-μm-thick GaSe electro-optic crystal rotated at an external angle of $\sim$ 50°. The focus $1/e^2$ diameters are 400 μm for both the mid-IR and gate beams. The average power of the gate beam incident on the EOS crystal is 180 mW, corresponding to $\sim$ 70 % of the crystal damage threshold. The gate and mid-IR beams are collimated after the crystal with an identical parabolic mirror. A short-pass filter at 950 nm is used to enhance the signal-to-noise ratio [23], and is followed by a quarter-waveplate, a Wollaston prism, and a pair of balanced photodiodes to detect the EOS signal.

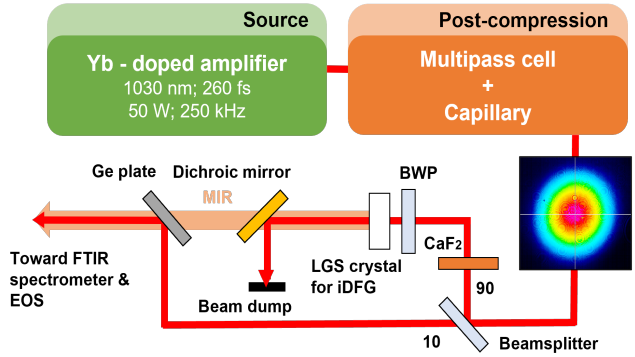

Fig. 1. Schematic of the experimental setup.

For an iDFG process that requires orthogonal polarization states for the pump and signal spectral parts, the input polarization on the nonlinear crystal is usually set at 45° from the desired orientation [7]. This divides the whole spectrum equally on the crystal axes, thereby wasting half the available photons. As depicted in Fig. 2, a suitable multi-order waveplate can separate all pump and signal photons onto the e and o axis of the LGS respectively thus doubling the number of pump and signal photons involved in the interaction.

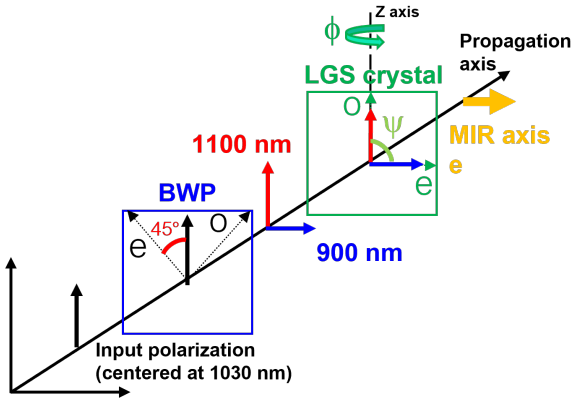

Fig. 2. Evolution of the polarization states along the propagation axis. The 1030 nm input beam polarization (black arrow) is at 45° with respect to the BWP axes. After the BWP, the pump (blue arrow) photons are rotated on the e axis of the LGS crystal. The signal (red arrow) polarization is unrotated. The mid-IR radiation (orange arrow) is generated on the e axis.

The NIR spectrum at the input of the BWP is shown in Fig. 3. It spans from 880 nm to 1160 nm at -20 dB. By carefully adjusting the thickness of the birefringent material, and taking into account the desired interacting central wavelengths, it is possible to design a waveplate that introduces a phase shift corresponding to N $\times$ λ (where N is integer and λ is the wavelength) on one part of the incident spectrum and to (N + 1/2) $\times$ λ on the other part of the incident spectrum. We choose a 255-μm-thick quartz plate as a birefringent material with a thickness of 255 μm, corresponding to N=2. When the incident polarization state is oriented at 45° from the waveplate axis, this results in an unrotated polarization for the signal at 1100 nm and a 90° rotation for the pump at 900 nm. Projected polarizations spectra on each axis of the LGS crystal after the BWP are plotted in Fig. 3. The measurement of the 90°-rotated spectrum has been performed using a polarizing beamsplitter made of a $\lambda/2$ waveplate and a Ge plate at Brewster's angle. As expected, only the short wavelengths of the spectrum are rotated at 90°, while the polarization of long wavelengths remains unrotated. To illustrate this, the inset of Fig. 3 shows the measured power fraction of rotated and unrotated polarizations as a function of wavelength. A simple simulation (red and blue colored lines, Fig. 3) based on the input spectrum and the full wavelength dependence of the ordinary and extraordinary indices of the BWP through Sellmeier equations shows excellent agreement with the measurements.

The corresponding measured and simulated temporal profiles of each polarization state at the output of the BWP are presented in Fig. 4. The Fourier-transform limited (FTL) duration corresponding to the 10.3 fs-long input pulse is 10.2 fs. The simulated pulse duration for the rotated and unrotated pulses are 14.8 fs (11 fs, FTL) and 16.5 fs (12.8 fs, FTL) respectively. This process introduces a small group velocity difference and group velocity dispersion, along with the duration increase that corresponds to spectral filtering. As the d-scan does not allow delay measurement between pulses, we have temporally shifted them to make the delay consistent with the simulation. We found the

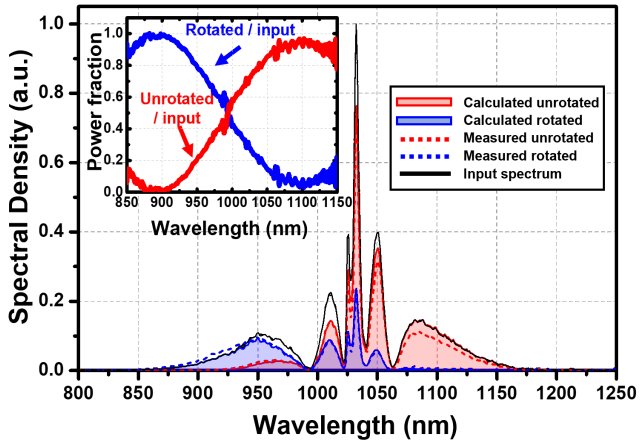

Fig. 3. Experimental spectrum at the input of the BWP (black line). Measured (red dashed lines) and calculated (red filled curve) unrotated spectra after the BWP. Measured (blue dashed lines) and calculated (blue filled curve) rotated spectra after the BWP. Inset: measured power fraction of rotated (blue line) and unrotated (red line) polarizations as a function of wavelength.

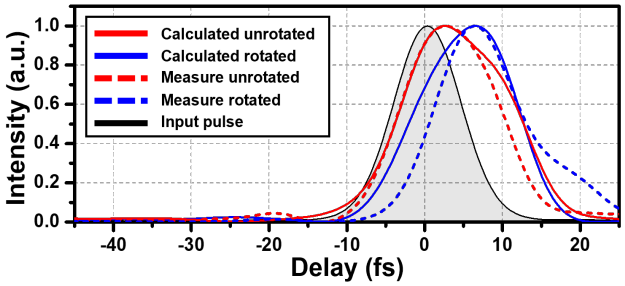

Fig. 4. Simulated rotated (blue line) and unrotated (red line) and measured rotated (blue dashed line) and unrotated (red dashed line) temporal intensity envelopes after propagation through the 255 μm-thick BWP. The grey filled curve is the FTL input pulse.

measured durations of the rotated and unrotated pulses to be 12.6 fs (11.2 fs, FTL) and 14.5 fs (14.1 fs, FTL), respectively. It confirms that the durations of the pulses on each polarization axis are increased by about 20% compared to the input one.

The iDFG setup is first operated in a standard configuration, without BWP. We fixed the phase matching angle ϕ and we optimize the ratio between the extraordinary/ordinary waves by turning the input polarization (angle ψ) while monitoring the iDFG idler power. The dependence of idler power (measured after the Ge plate) on the input polarization angle is shown in Fig. 5. Local maxima are reached each time the input polarization is at 45° with the crystal axes. One can notice that idler power does not reach zero, which might be explained by an imperfect cut of the crystal or input polarization state. This result indicates that, in our experimental conditions, without BWP, the iDFG process is most efficient when the input power is equally distributed between the crystal axes. The maximum generated mid-IR average power after the Ge plate is 8.1 mW. We estimate the generated mid-IR power directly after the crystal to be 12.9 mW considering the Fresnel reflections at the interfaces with air

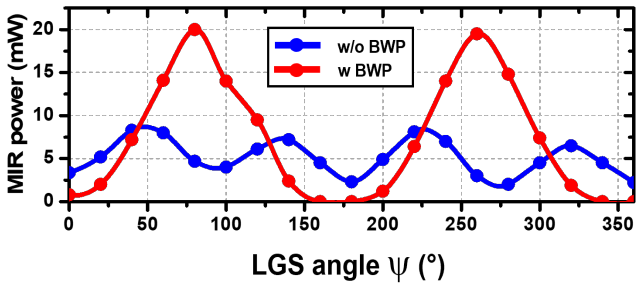

Fig. 5. Dependence of the mid-IR idler beam average power on the polarization angle of the driving NIR beam measured without BWP (blue line) and with BWP (red line) for a 1 mm-thick LGS crystal.

for the crystal, the dichroic mirror and the Ge plate.

The BWP is now inserted before the LGS crystal. We optimize the mid-IR average power with the same method described above, while the angle between the input polarization and the axes of the BWP is set to 45°. We then proceed to the same measurement by tuning the angle between the incident polarization and the crystal axes. The result is shown in Fig. 5. As expected, only two peaks appear, each spaced by 180°. Indeed, only the two angles corresponding to the pump and the signal waves on the e and o axes respectively are capable to generate mid-IR radiation efficiently according to the phase matching condition.

The idler average power reaches 20 mW (31.8 mW considering different losses as described above) corresponding to an increase by a factor 2.5 compared to the configuration without the BWP. We carried out additional measurements with other LGS crystals of different thicknesses (0.5 and 2 mm). These results, shown in Table 1, indicate that we optimize the number of photons enrolled in the nonlinear interaction within the crystals.

In the following, we report on the temporal and spectral properties of the generated mid-IR beam. Fig. 6 shows the measured EOS trace corresponding to the mid-IR pulse delivered using the 1-mm-thick LGS crystal. The trace has been obtained by scanning the time delay at a frequency of 2 Hz, and averaging 5 consecutive scans, corresponding to a total acquisition time of 2.5 s. The replicas observed 450 fs before and 400 fs after the main pulse are attributed respectively to replicas of the gate and mid-IR pulses after an additional round trip in the GaSe crystal. The slightly larger value of the delay observed for the gate pulse with respect to the mid-IR pulse is consistent with the expected difference in group velocities. These replicas are strongly attenuated when plotting the pulse intensity (see inset of Fig. 6). The corresponding pulse duration is 64 fs, close to the Fourier transform limited pulse duration of 55.6 fs, and corresponding to 2.4 optical cycles at the central wavelength of 8.6 µm.

Table 1. Mid-IR average powers and yields with and without BWP for different LGS thicknesses

	Average power (mW)		Efficiency (%)		
LGS (mm)	w/o BWP	w BWP	w/o BWP	w BWP	BWP factor
0.5	3.3	10.3	0.03	0.08	3.1
1	8.1	20	0.07	0.16	2.5
2	13	37	0.1	0.3	2.8

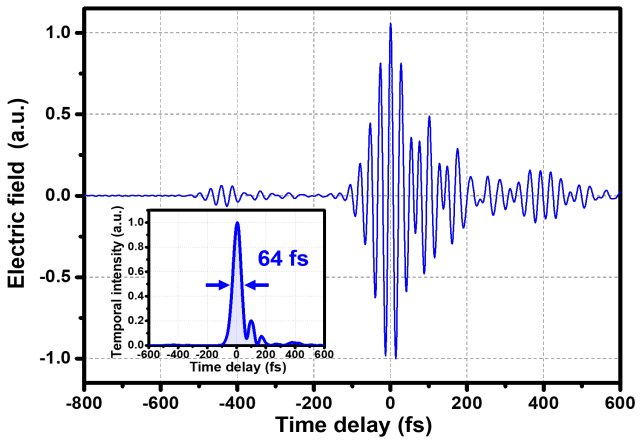

Fig. 6. Electro-optic sampling (EOS) trace of the mid-IR pulse corresponding to the spectrum centered at 8.6 µm in Fig. 7. Inset: temporal intensity of the EOS trace.

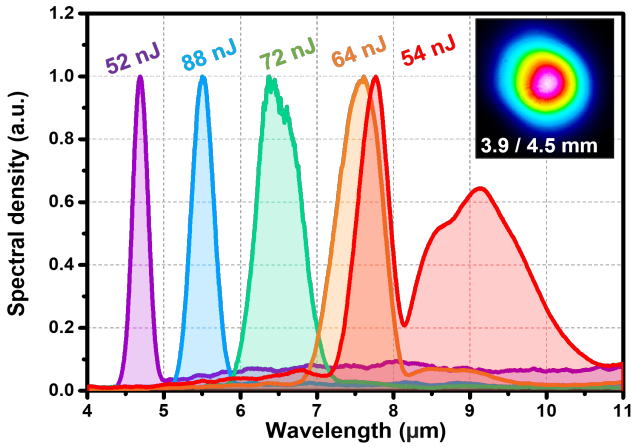

Fig. 7. Tunability of the mid-IR spectrum for the 1 mm-thick LGS crystal. The spectra are obtained after 10 averages. Inset: output mode of the mid-IR spectrum centered at 8.6 µm.

Finally, measurements are carried out to study the tunability of the spectrum by slightly rotating the LGS crystal around the angle ϕ. Fig. 7 shows the result: the mid-IR spectrum is tunable over a bandwidth extending from 4.5 to 9.5 μm, while maintaining the average power above half of its maximum. The generated spectra are narrower as the central wavelength decreases because of the phase-matching properties of LGS. The spectra obtained with and without (not shown) the BWP are almost identical. We measured the mode of the mid-IR (see inset of Fig. 7) corresponding to the spectrum centered at 8.6 µm Fig. 7. The ellipticity of the beam is 89 %.

To conclude, we demonstrate an increase of the mid-IR average power generated through iDFG by a factor ≥ 2.5 using a simple waveplate that performs spectrally dependent polarization rotation. The iDFG efficiency reaches 0.16 % instead of 0.07 % without BWP for the 1 mm-thick LGS crystal. The BWP can be made with a wide variety of birefringent materials (calcite, quartz, yttrium or gadolinium vanadate for example) as long as the concerned material is transparent for both NIR wavelengths (pump and signal) involved in the nonlinear interaction. Likewise, the use of this BWP applies to all types of nonlinear crystals used to generate mid-IR via iDFG (LGS, BGS, GaSe, AGGS, AGS, LIS, LGN, ZGP as instances), regardless of the central wavelength of the incident pulse (for example around 800 nm, 1030 nm, or 2000 nm for Ti:Sa, ytterbium-based, and thulium-based sources), when the phase matching condition requires the interaction of a pump and an orthogonally polarized signal. This technique should facilitate the design of high power, broad bandwidth, CEP-stable mid- and far- infrared sources.

Funding. Agence Nationale de la Recherche (ANR) (ANR-10-LABX-0039-PALM, ANR-19-CE30-0001-MIRTHYX).

Disclosures. The authors declare no conflicts of interest.

REFERENCES

1. A. Bonvalet, M. Joffre, J. Martin, and A. Migus, Appl. Phys. Lett. **67**, 2907 (1995).
2. R. Kaindl, D. Smith, M. Joschko, M. Hasselbeck, M. Woerner, and T. Elsaesser, Opt. letters **23**, 861 (1998).
3. R. Huber, A. Brodschelm, F. Tauser, and A. Leitenstorfer, Appl. Phys. Lett. **76**, 3191 (2000).
4. L. Lavenu, M. Natile, F. Guichard, X. Délen, M. Hanna, Y. Zaouter, and P. Georges, Opt. express **27**, 1958 (2019).
5. S. Hädrich, M. Kienel, M. Müller, A. Klenke, J. Rothhardt, R. Klas, T. Gottschall, T. Eidam, A. Drozdy, P. Jójárt *et al.*, Opt. letters **41**, 4332 (2016).
6. M. Gebhardt, C. Gaida, T. Heuermann, F. Stutzki, C. Jauregui, J. Antonio-Lopez, A. Schulzgen, R. Amezcua-Correa, J. Limpert, and A. Tünnermann, Opt. letters **42**, 4179 (2017).
7. C. Gaida, M. Gebhardt, T. Heuermann, F. Stutzki, C. Jauregui, J. Antonio-Lopez, A. Schülzgen, R. Amezcua-Correa, A. Tünnermann, I. Pupeza *et al.*, Light. Sci. & Appl. **7**, 1 (2018).
8. T. Butler, N. Lilienfein, J. Xu, N. Nagl, C. Hofer, D. Gerz, K. Mak, C. Gaida, T. Heuermann, M. Gebhardt *et al.*, J. Physics: Photonics **1**, 044006 (2019).
9. I. Pupeza, D. Sánchez, J. Zhang, N. Lilienfein, M. Seidel, N. Karpowicz, T. Paasch-Colberg, I. Znakovskaya, M. Pescher, W. Schweinberger *et al.*, Nat. Photonics **9**, 721 (2015).
10. K. Kato, K. Miyata, L. Isaenko, S. Lobanov, V. Vedenyapin, and V. Petrov, Opt. letters **42**, 4363 (2017).
11. I. Pupeza, M. Huber, M. Trubetskov, W. Schweinberger, S. A. Hussain, C. Hofer, K. Fritsch, M. Poetzlberger, L. Vamos, E. Fill *et al.*, Nature **577**, 52 (2020).
12. Z. Heiner, L. Wang, V. Petrov, and M. Mero, Opt. express **27**, 15289 (2019).
13. S. B. Penwell, L. Whaley-Mayda, and A. Tokmakoff, Opt. letters **43**, 1363 (2018).
14. B.-H. Chen, E. Wittmann, Y. Morimoto, P. Baum, and E. Riedle, Opt. express **27**, 21306 (2019).
15. S. Vasilyev, I. S. Moskalev, V. O. Smolski, J. M. Peppers, M. Mirov, A. V. Muraviev, K. Zawilski, P. G. Schunemann, S. B. Mirov, K. L. Vodopyanov *et al.*, Optica **6**, 111 (2019).
16. Q. Wang, J. Zhang, A. Kessel, N. Nagl, V. Pervak, O. Pronin, and K. F. Mak, Opt. letters **44**, 2566 (2019).
17. N. Ishii, P. Xia, T. Kanai, and J. Itatani, Opt. express **27**, 11447 (2019).
18. J. Liu, J. Ma, D. Lu, X. Gu, Z. Cui, P. Yuan, J. Wang, G. Xie, H. Yu, H. Zhang *et al.*, Opt. Lett. **45**, 5728 (2020).
19. H. Fattahi, A. Schwarz, S. Keiber, and N. Karpowicz, Opt. letters **38**, 4216 (2013).
20. K. Kaneshima, N. Ishii, K. Takeuchi, and J. Itatani, Opt. express **24**, 8660 (2016).
21. M. Miranda, P. Rudawski, C. Guo, F. Silva, C. L. Arnold, T. Binhammer, H. Crespo, and A. L'Huillier, "Ultrashort laser pulse characterization from dispersion scans: a comparison with spider," in *CLEO: Science and Innovations,* (Optical Society of America, 2013), pp. JTh2A–31.
22. A. Weigel, P. Jacob, D. Gröters, T. Buberl, M. Huber, M. Trubetskov, J. Heberle, and I. Pupeza, Opt. Express **29**, 20747 (2021).
23. M. Porer, J.-M. Ménard, and R. Huber, Opt. letters **39**, 2435 (2014).

FULL REFERENCES

1. A. Bonvalet, M. Joffre, J. Martin, and A. Migus, "Generation of ultrabroadband femtosecond pulses in the mid-infrared by optical rectification of 15 fs light pulses at 100 mhz repetition rate," Appl. Phys. Lett. **67**, 2907–2909 (1995).
2. R. Kaindl, D. Smith, M. Joschko, M. Hasselbeck, M. Woerner, and T. Elsaesser, "Femtosecond infrared pulses tunable from 9 to 18?? μm at an 88-mhz repetition rate," Opt. letters **23**, 861–863 (1998).
3. R. Huber, A. Brodschelm, F. Tauser, and A. Leitenstorfer, "Generation and field-resolved detection of femtosecond electromagnetic pulses tunable up to 41 thz," Appl. Phys. Lett. **76**, 3191–3193 (2000).
4. L. Lavenu, M. Natile, F. Guichard, X. Délen, M. Hanna, Y. Zaouter, and P. Georges, "High-power two-cycle ultrafast source based on hybrid nonlinear compression," Opt. express **27**, 1958–1967 (2019).
5. S. Hädrich, M. Kienel, M. Müller, A. Klenke, J. Rothhardt, R. Klas, T. Gottschall, T. Eidam, A. Drozdy, P. Jójárt *et al.*, "Energetic sub-2-cycle laser with 216 w average power," Opt. letters **41**, 4332–4335 (2016).
6. M. Gebhardt, C. Gaida, T. Heuermann, F. Stutzki, C. Jauregui, J. Antonio-Lopez, A. Schulzgen, R. Amezcua-Correa, J. Limpert, and A. Tünnermann, "Nonlinear pulse compression to 43 w gw-class few-cycle pulses at 2 μm wavelength," Opt. letters **42**, 4179–4182 (2017).
7. C. Gaida, M. Gebhardt, T. Heuermann, F. Stutzki, C. Jauregui, J. Antonio-Lopez, A. Schülzgen, R. Amezcua-Correa, A. Tünnermann, I. Pupeza *et al.*, "Watt-scale super-octave mid-infrared intrapulse difference frequency generation," Light. Sci. & Appl. **7**, 1–8 (2018).
8. T. Butler, N. Lilienfein, J. Xu, N. Nagl, C. Hofer, D. Gerz, K. Mak, C. Gaida, T. Heuermann, M. Gebhardt *et al.*, "Multi-octave spanning, watt-level ultrafast mid-infrared source," J. Physics: Photonics **1**, 044006 (2019).
9. I. Pupeza, D. Sánchez, J. Zhang, N. Lilienfein, M. Seidel, N. Karpowicz, T. Paasch-Colberg, I. Znakovskaya, M. Pescher, W. Schweinberger *et al.*, "High-power sub-two-cycle mid-infrared pulses at 100 mhz repetition rate," Nat. Photonics **9**, 721–724 (2015).
10. K. Kato, K. Miyata, L. Isaenko, S. Lobanov, V. Vedenyapin, and V. Petrov, "Phase-matching properties of ligas 2 in the 1.025–10.5910 μm spectral range," Opt. letters **42**, 4363–4366 (2017).
11. I. Pupeza, M. Huber, M. Trubetskov, W. Schweinberger, S. A. Hussain, C. Hofer, K. Fritsch, M. Poetzlberger, L. Vamos, E. Fill *et al.*, "Field-resolved infrared spectroscopy of biological systems," Nature **577**, 52–59 (2020).
12. Z. Heiner, L. Wang, V. Petrov, and M. Mero, "Broadband vibrational sum-frequency generation spectrometer at 100 khz in the 950-1750 cm- 1 spectral range utilizing a ligas 2 optical parametric amplifier," Opt. express **27**, 15289–15297 (2019).
13. S. B. Penwell, L. Whaley-Mayda, and A. Tokmakoff, "Single-stage mhz mid-ir opa using ligas 2 and a fiber laser pump source," Opt. letters **43**, 1363–1366 (2018).
14. B.-H. Chen, E. Wittmann, Y. Morimoto, P. Baum, and E. Riedle, "Octave-spanning single-cycle middle-infrared generation through optical parametric amplification in ligas 2," Opt. express **27**, 21306–21318 (2019).
15. S. Vasilyev, I. S. Moskalev, V. O. Smolski, J. M. Peppers, M. Mirov, A. V. Muraviev, K. Zawilski, P. G. Schunemann, S. B. Mirov, K. L. Vodopyanov *et al.*, "Super-octave longwave mid-infrared coherent transients produced by optical rectification of few-cycle 2.5-μm pulses," Optica **6**, 111–114 (2019).
16. Q. Wang, J. Zhang, A. Kessel, N. Nagl, V. Pervak, O. Pronin, and K. F. Mak, "Broadband mid-infrared coverage (2–17 μm) with few-cycle pulses via cascaded parametric processes," Opt. letters **44**, 2566–2569 (2019).
17. N. Ishii, P. Xia, T. Kanai, and J. Itatani, "Optical parametric amplification of carrier-envelope phase-stabilized mid-infrared pulses generated by intra-pulse difference frequency generation," Opt. express **27**, 11447–11454 (2019).
18. J. Liu, J. Ma, D. Lu, X. Gu, Z. Cui, P. Yuan, J. Wang, G. Xie, H. Yu, H. Zhang *et al.*, "Few-cycle pulses tunable from 3 to 7 μm via intrapulse difference-frequency generation in oxide lgn crystals," Opt. Lett. **45**, 5728–5731 (2020).
19. H. Fattahi, A. Schwarz, S. Keiber, and N. Karpowicz, "Efficient, octave-spanning difference-frequency generation using few-cycle pulses in simple collinear geometry," Opt. letters **38**, 4216–4219 (2013).
20. K. Kaneshima, N. Ishii, K. Takeuchi, and J. Itatani, "Generation of carrier-envelope phase-stable mid-infrared pulses via dual-wavelength optical parametric amplification," Opt. express **24**, 8660–8665 (2016).
21. M. Miranda, P. Rudawski, C. Guo, F. Silva, C. L. Arnold, T. Binhammer, H. Crespo, and A. L'Huillier, "Ultrashort laser pulse characterization from dispersion scans: a comparison with spider," in *CLEO: Science and Innovations,* (Optical Society of America, 2013), pp. JTh2A–31.
22. A. Weigel, P. Jacob, D. Gröters, T. Buberl, M. Huber, M. Trubetskov, J. Heberle, and I. Pupeza, "Ultra-rapid electro-optic sampling of octave-spanning mid-infrared waveforms," Opt. Express **29**, 20747–20764 (2021).
23. M. Porer, J.-M. Ménard, and R. Huber, "Shot noise reduced terahertz detection via spectrally postfiltered electro-optic sampling," Opt. letters **39**, 2435–2438 (2014).